DOI:10.3969/j.issn.1005-202X.2017.07.001

医学影像物理

Background correction methods in X-ray phase-contrast imaging with Talbot-Lau interferometer: a comparative study

YANG Meng[1], HU Renfang[1], WANG Shenghao[2], WU Zhao[1], TIAN Yangchao[1]

1. National Synchrotron Radiation Laboratory, University of Science and Technology of China, Hefei 230027, China; 2. Key Laboratory of Materials for High-Power Laser, Shanghai Institute of Optics and Fine Mechanics, Chinese Academy of Sciences, Shanghai 201800, China

Abstract: In X-ray phase-contrast imaging with Talbot-Lau interferometer, a background correction process has to be performed to obtain the pure signal of the sample. In this study, we tested the performances of different background correction strategies and proposed a novel background correction method, [arg(S)-arg(B)] cyclic shift, in which the initial phase of each pixel is changed by a cyclic shift operation on the raw image data from phase step-scan. Both experimental results and numerical analysis showed that the improved method could successfully realize background correction without error. In addition, the effective phase measuring range of this method allowed flexible tuning within (-π+3, π+3], as compared with the fixed effective measuring range of (-π, π] in the conventional methods.

Keywords: X-ray imaging; Talbot-Lau interferometer; background correction; cyclic shift; phase unwrapping

Introduction

X-ray phase-contrast imaging, which uses phase shift as the imaging signal, can provide remarkably improved contrast over conventional absorption-based imaging for weakly absorbing samples, such as biological soft tissues composed of low-atomic-number elements (C, H, N, O, et al) and fibre composites[1-3]. In the past 50 years, several X-ray phase-contrast imaging methods have been proposed[4-13], but none of them has so far found wide applications in medical or industrial areas, where a laboratory X-ray source and a large field of view are highly required. The application of a Talbot-Lau interferometer in the hard X-ray region with a conventional low-brilliance X-ray source can be considered as a great breakthrough in X-ray phase-contrast imaging[14-16], because it allows the use of a low-brilliance X-ray tube to remove the constraints of radiation source and micro-focus source that hinders the wide use of phase-contrast X-ray radiography and tomography. Many potential applications of X-ray phase-contrast imaging with Talbot-Lau interferometer in biomedical imaging have been studied[17-21].

In X-ray phase-contrast imaging with an X-ray Talbot-Lau interferometer, a background correction process is essential to obtain the pure phase signals of the sample[13, 22]. In a typical scenario, two phase step-scan is carried out either with or without sample in the beam path, and in subsequent data post-processing, two conventional background correction methods, listed below as formula (1) and (2), were usually used to retrieve the refraction angle from the two sets of raw data.

$$\varphi(x,y)=\frac{d}{2\pi\times z_T}\times\arg\left\{\frac{\sum_{k=0}^{M-1}[I^s_{k+1}(x,y,z_T)\times\exp(-i2\pi\frac{k}{M})]}{\sum_{k=0}^{M-1}[I^b_{k+1}(x,y,z_T)\times\exp(-i2\pi\frac{k}{M})]}\right. \quad (1)$$

$$\varphi(x,y)=\frac{d}{2\pi\times z_T}\times\left\{\begin{array}{l}\arg\sum_{k=0}^{M-1}[I^s_{k+1}(x,y,z_T)\times\exp(-i2\pi\frac{k}{M})]-\\ \arg\sum_{k=0}^{M-1}[I^b_{k+1}(x,y,z_T)\times\exp(-i2\pi\frac{k}{M})]\end{array}\right. \quad (2)$$

where z_T is the distance between gratings G1 and G2 (when the sample is placed between gratings G0 and G1); d stands for the period of the grating G2; $I^s_{k+1}(m,n)$ and $I^b_{k+1}(m,n)$ are the gray values of the pixel (m,n) at the $(k+1)^{th}$ step of the phase step-scan with and without sample, respectively; M is the number of steps during the phase step-scan in one period of grating G2, and $1\leqslant k+1\leqslant M$.

Received: 2017-03-14

Supported by National Research and Development Projects for Key Scientific Instruments (CZBZDYZ20140002) and Fundamental Research Funds for the Central Universities (WK2310000065)

Leading authors: YANG Meng, male, master, research direction: X-ray phase contrast imaging, E-mail: henry@mail.ustc.edu.cn; HU Renfang, male, doctor, research direction: X-ray phase contrast imaging, E-mail: hurf@mail.ustc.edu.cn

Corresponding author: TIAN Yangchao, E-mail: ychtian@ustc.edu.cn; WANG Shenghao, male,doctor, assistant professor, research direction: X-ray phase contrast imaging, E-mail: wangshenghao@siom.ac.cn

In the following text, we refer to formula (1) as arg (S/B) method and formula (2) as arg(S)-arg(B) method. These two methods, though appearing equivalent in mathematics, produce differences in X-ray phase contrast imaging with a Talbot-Lau interferometer. The arg(S)-arg (B) method has an effective phase measuring range of $(-2\pi, 2\pi]$, but phase wrapping often occurs even for a very small phase shift caused by the sample; for this reason, arg (S/B) method is more widely used than arg(S)- arg(B) method in data post-processing. In contrast, the arg(S/B) method has a fixed effective phase measuring range of $(-\pi, \pi]$, and when the expected phase exceeds this range, phase wrapping would occur and a complex phase unwrapping algorithm has to be used[23-27]. The combination of these two methods that exploits their advantages and meanwhile avoids their limitations is thus interesting and meaningful.

In this study, we displayed the layout of an X-ray Talbot-Lau interferometer, and compared the performance of arg(S)- arg(B) method and arg(S/B) method in the processing of a phase step-scan dataset. We analyzed the source of errors in arg(S)-arg(B) method and proposed a new background correction method based on the theory of circle shift operation. The performance of this new method was evaluated in comparison with arg(S)-arg(B) method and arg(S/B) method to demonstrate the advantages of this new background correction method.

1 Materials and methods

1.1 Experimental setup

The X-ray phase-contrast imaging with a Talbot-Lau interferometer was carried out at the Institute of Multidisciplinary Research for Advanced Materials, Tohoku University, Japan. Fig.1 is the schematic illustration of this X-ray interferometer, which consists mainly of an X-ray tube, an X-ray detector and 3 micro-structured gratings, all assembled on multi-dimensional motorized optical displacement tables. The X- ray is generated from a tungsten rotating anode X-ray source. The source grating G0 with a period of 22.7 μm and a gold height of 70 μm is positioned at a distance of 50 mm from the emission point inside the X-ray source, and the beam splitter grating G1 with a period of 4.36 μm and a Si height of 2.43 μm, which can induce a phase shift of $\pi/2$ at approximately 27 keV, is placed at a distance of 106.9 mm from G0 behind the gantry axis; the sample is mounted closely before G1. The analyzing grating G2 with a period of 5.4 μm and a gold height of 65 μm is positioned in contact with the detector, and the distance between G1 and G2 is 25.6 mm, corresponding to the first order integer Talbot distance of grating G1. The X-ray images are captured using a charge coupled device with an effective receiving area of (68.4×68.4) mm^2 and a pixel size of (18×18) μm^2.

As illustrated in Fig.1, the differential phase-contrast image information processing essentially relies on the fact that the beam will appear slightly refracted when passing through the sample placed in the X-ray beam path, and the fundamental rationale of differential phase- contrast imaging depends on local detection of the angular deviation α . Determination of the refraction angle can be achieved by combining the Moire fringe and phase-stepping technique [28-29]. Further details of the theoretical basis of X- ray phase- contrast imaging using grating interferometer are referred to previous documentations[12-14, 30].

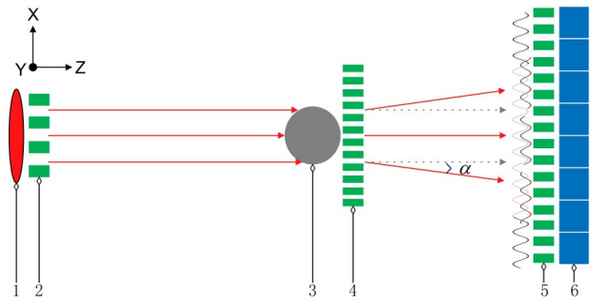

1: X-ray source; 2: Source grating (G0); 3: Sample; 4: Beam splitter grating (G1); 5: Analyzing grating (G2); 6: X-ray detector

Fig.1 Schematic illustration of an X−ray Talbot−Lau interferometer

1.2 Image acquisition

The sample we used is a POM cylinder (10 mm in diameter and about 90 mm in length), a PMMA cylinder (5 mm in diameter and about 100 mm in length) and a POM cylinder (5 mm in diameter and about 80 mm in length). During the experiment, the X-ray generator was operated at a tube current of 45 mA and a tube voltage of 40 kV. After the fine alignment of the 3 gratings and the sample, 5 steps in one period of grating G2 were adopted for phase step-scan; and for each step, 20 seconds was allowed for capturing a raw image, and the same phase

step-scan was performed after removing the sample. The 5 positions of grating maintained the same in the scans either with or without a sample in the beam path using a high-precision optical displacement table.

2 Background correction using conventional methods

2.1 Background correction using arg(S/B) method and arg(S)-arg(B) method

Fig.2 shows the raw images from two phase step-scan. S ①, S ②, S ③, S ④ and S ⑤ are the 5 raw images with sample in the beam path, while B ①, B ②, B ③, B ④ and B ⑤ are the images without sample in the beam path. In the 5 background images without sample, the light intensity does not appear uniform with large Moire fringes. Obtaining a flat background using an X-ray Talbot-Lau interferometer is almost impossible because of the poor conditions of the X-ray gratings and their alignment.

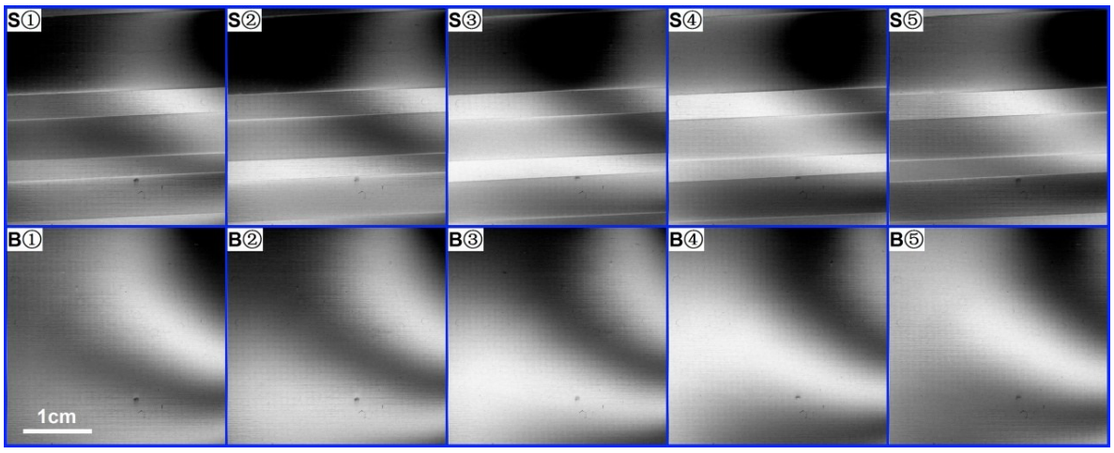

S ①, S ②, S ③, S ④, S ⑤ are the raw images with sample in the beam path, and B ①, B ②, B ③, B ④, B ⑤ are the raw images without sample in the beam path. In each image with sample, the POM cylinder (Φ =10 mm), PMMA cylinder (Φ =5 mm) and POM cylinder (Φ =5 mm) are presented from the top to bottom. The analyzing grating were positioned successively at positions ①②③④⑤, which were equally spaced by *d*/5 (*d* is the period of the analyzing grating). All the images were windowed for the optimized appearance with a linear gray scale.

Fig.2 Raw images of the phase step−scan

Two conventional methods, namely arg(S/B) method and arg(S)- arg(B) method, were used separately to compute the refraction image of the sample. Fig.3a is the refraction image computed with arg(S)-arg(B) method, and Fig.3b is that processed with arg(S/B) method. Fig.3c and Fig.3d present the enlarged view of the boxed area chosen from the same position in Fig.3a and Fig.3b, respectively. The images show obvious differences in the refraction images computed with the two methods, for instance, the gray values of the pixels P1 and S1 in Fig.3c are obviously different from those of the corresponding pixels (P2 and S2) in Fig.3d. According to the known information of the sample, we conclude that a correct result can be obtained with arg(S/B) method, and the refraction signals in many areas of the image obtained with arg(S)-arg(B) method are incorrect.

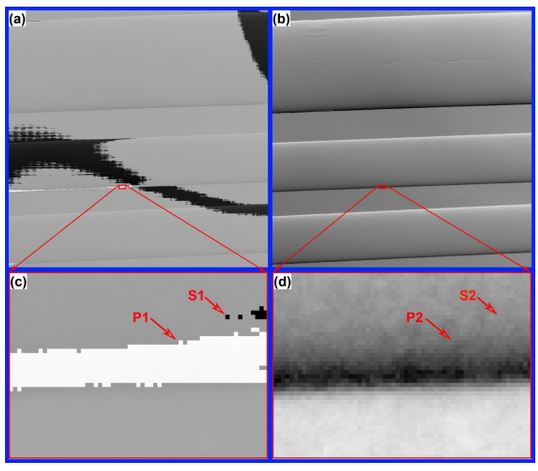

Fig.3a and Fig.3b are the results processed with arg(S)-arg(B) and arg(S/B) methods, respectively; Fig.3c and Fig.3d are the enlarged view of the boxed areas chosen from the same position in Fig.3a and Fig.3b, respectively. All the images are windowed for the optimized appearance with a linear gray scale.

Fig.3 X−ray refraction image of the sample

2.2 Error sources in images computed with arg(S)-arg(B) method

To identify the sources of errors in the image computed with arg(S)- arg(B) method, we traced the computation processes of the refraction angle at pixel P1 in Fig.3c and at pixel P2 in Fig.3d (P1 and P2 were taken from the same position in the images). The computation processes for P1 and P2 are presented in the following formula (3) and formula (4), respectively.

$$\begin{aligned}\varphi_{P1} &= \frac{d}{2\pi \times z_T} \times \left\{ \begin{array}{l} \arg\sum_{k=0}^{4}[I^{s}_{k+1}(x,y,z_T) \times \exp(-i2\pi\frac{k}{5})] - \\ \arg\sum_{k=0}^{4}[I^{b}_{k+1}(x,y,z_T) \times \exp(-i2\pi\frac{k}{5})] \end{array} \right\} \\ &= \frac{d}{2\pi \times z_T} \times \left\{ \begin{array}{l} \arg[-3\,629.9 + 66.949\,7\,i] - \\ \arg[-3\,899.72 - 499.816\,i] \end{array} \right\} \\ &= \frac{d}{2\pi \times z_T} \times \{3.123\,15 - (-3.014\,12)\} \\ &= \frac{d}{2\pi \times z_T} \times 6.137\,27 \end{aligned} \tag{3}$$

$$\begin{aligned}\varphi_{P2} &= \frac{d}{2\pi \times z_T} \times \arg\left\{ \frac{\sum_{k=0}^{4}[I^{s}_{k+1}(x,y,z_T) \times \exp(-i2\pi\frac{k}{5})]}{\sum_{k=0}^{4}[I^{b}_{k+1}(x,y,z_T) \times \exp(-i2\pi\frac{k}{5})]} \right\} \\ &= \frac{d}{2\pi \times z_T} \times \arg\left\{ \frac{-3\,629.9 + 66.949\,7\,i}{-3\,899.72 - 499.816\,i} \right\} \\ &= \frac{d}{2\pi \times z_T} \times \arg\{0.913\,604 - 0.134\,262\,i\} \\ &= \frac{d}{2\pi \times z_T} \times (-0.145\,914) \end{aligned} \tag{4}$$

Similarly, the computation processes for the refraction information of pixels S1 in Fig.3c and S2 in Fig.3d (S1 and S2 were taken from the same position in images) are shown in formula (5) and formula (6) as the following, respectively.

$$\begin{aligned}\varphi_{S1} &= \frac{d}{2\pi \times z_T} \times \left\{ \begin{array}{l} \arg\sum_{k=0}^{4}[I^{s}_{k+1}(x,y,z_T) \times \exp(-i2\pi\frac{k}{5})] - \\ \arg\sum_{k=0}^{4}[I^{b}_{k+1}(x,y,z_T) \times \exp(-i2\pi\frac{k}{5})] \end{array} \right\} \\ &= \frac{d}{2\pi \times z_T} \times \left\{ \begin{array}{l} \arg[-4\,044.07 - 252.068\,i] - \\ \arg[-4\,411.39 + 80.125\,8\,i] \end{array} \right\} \\ &= \frac{d}{2\pi \times z_T} \times \{-3.079\,34 - 3.123\,43\} \\ &= \frac{d}{2\pi \times z_T} \times (-6.202\,77) \end{aligned} \tag{5}$$

$$\begin{aligned}\varphi_{S2} &= \frac{d}{2\pi \times z_T} \times \arg\left\{ \frac{\sum_{k=0}^{4}[I^{s}_{k+1}(x,y,z_T) \times \exp(-i2\pi\frac{k}{5})]}{\sum_{k=0}^{4}[I^{b}_{k+1}(x,y,z_T) \times \exp(-i2\pi\frac{k}{5})]} \right\} \\ &= \frac{d}{2\pi \times z_T} \times \arg\left\{ \frac{-4\,044.07 - 252.068\,i}{-4\,411.39 + 80.125\,8\,i} \right\} \\ &= \frac{d}{2\pi \times z_T} \times \arg\{0.915\,393 + 0.073\,766\,7\,i\} \\ &= \frac{d}{2\pi \times z_T} \times 0.080\,411 \end{aligned} \tag{6}$$

Comparisons between formula (3) and formula (4) and between formula (5) and formula (6) confirmed the differences between the images obtained by arg(S)-arg(B) method and arg(S/B) method. The computed phase of pixels P1 and S1 in Fig.3c were 6.108 67 and -6.123 55, respectively. As mentioned earlier, the effective phase measuring range of arg(S)-arg(B) method is (-2π, 2π], which explains why the pixel P1 in gray value image Fig. 3c features ultra-white while pixel S1 displays ultra-black.

Fig.4 presents a clear explanation of the error sources in arg(S)-arg(B) method. The blue sinusoid curve in Fig. 4a illustrates the relationship between the intensity of a given pixel in the detector and the position of the analyzing grating (we term it shift curve) without sample in the beam path, and the black one represents the shift curve with sample. The lateral shift of the curve was caused by the refraction of the beam when it passed through the sample, which was the fundamental principle of signal retrieval in X-ray phase-contrast imaging with Talbot and Talbot- Lau interferometer. We ignored the absorption and scattering effects of the sample when generating the curve. The blue saw tooth curve in Fig.4b presents the corresponding retrieved phase of the pixel computed by formula (7).

$$\varphi(x,y) = \arg\sum_{k=0}^{M-1}[I_{k+1}(x,y,z_T) \times \exp(-i2\pi\frac{k}{M})] \tag{7}$$

A one-to-one relationship is highlighted between the blue sinusoid curve in Fig.4a and the saw tooth curve in Fig.4b. For example, the 1st step of the phase step-scan was located at point A in the shift curve, and the 2nd, 3rd, 4th and 5th steps were successively and equally spaced by *d*/5 at the right of point A in the curve (*d* was the period of the analyzing grating G2). The retrieved phase of this pixel computed by formula (7) is the ordinate value of point B in the saw tooth curve shown in Fig.4b. Here we assumed that without sample in the beam path, the phase (arg(B)) of the pixel is π-0.1π, and after moving the sample into the beam path, we hypothesized that the shift curve of this pixel is laterally shifted by less than a period (as shown by the black sinusoid curve in Fig.4a). Because the positions of the analyzing grating G2 remained the same in the phase step-scan with sample as in scans without sample, the 1st step of the pixel with sample was located at point C in the black shift curve; obviously, the phase of point C in the black curve was equal to that of point D in the blue shift curve. Based on the aforementioned one- to- one relationship, the phase of this pixel with sample is the

ordinate value of point E as shown in Fig. 4(b), and here the phase (arg(S)) is assumed to be -π+0.3π. Using arg(S)-arg(B) method, we found that the pure phase of the sample at this pixel was -2π+0.4π, which was obviously wrong because the actual phase introduced by the sample was 0.4π. The error was due to the discontinuous nature of the saw tooth curve, and errors of this type was also known as the phase wrapping effect because the observed phase is φ modulo 2π (where φ is the real phase).

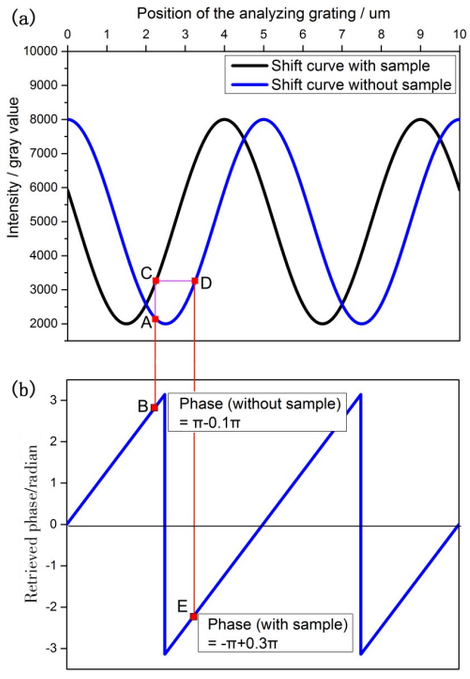

Fig.4a: Shift curve representing the relationship between the intensity of a given pixel in the detector and the position of the analyzing grating; Fig.4b: Corresponding retrieved phase of the pixel.

Fig.4 Explanation for the sources of error in the image computed with arg(S)−arg(B) method

2.3 Phase unwrapping solution for arg(S)-arg(B) method

［arg(S)-arg(B)］modulo 2π is expressed as formula (8).

$$[\arg(S)-\arg(B)]\text{modulo}2\pi=\arg(S)-\arg(B)+2k\pi \quad (8)$$

Where $k\in Z$, forcing $-\pi<\arg(S)-\arg(B)+2k\pi\leqslant\pi$.

The correct refraction angle at pixel P1 and S1 were calculated using the phase unwrapping solution:

$$\begin{aligned}\varphi^{*}_{P1}&=\frac{d}{2\pi\times z_T}\times(6.137\,27\text{modulo}2\pi)\\&=\frac{d}{2\pi\times z_T}\times(-0.145\,915)=\varphi_{P2}\end{aligned} \quad (9)$$

$$\begin{aligned}\varphi^{*}_{S1}&=\frac{d}{2\pi\times z_T}\times(-6.202\,77\text{modulo}2\pi)\\&=\frac{d}{2\pi\times z_T}\times 0.080\,415\,3=\varphi_{S2}\end{aligned} \quad (10)$$

3 A new background correction method based on arg(S)-arg(B) method

3.1 Strategy of cyclic shift operation on the raw images

The new background correction method we propose herein is based on the cyclic shift operation on the raw images. As shown in Fig.5, the blue sinusoid curve in Fig.5a and the blue saw tooth curve in Fig.5b share the same one-to-one relationship as that in Fig.4. Supposedly, in phase step- scan without samples in the beam path, analyzing grating was positioned successively at positions ①②③④⑤ (which were equally spaced by *d*/5)in the shift curve, inputting the images in order of ①②③④⑤ to formula (7) results in a retrieved phase of a given pixel equivalent to the ordinate value of point T1 shown in Fig.5b. Incyclic shift operation, changing the order of the images from ①②③④⑤ to ⑤①②③④ results in a retrieved phase, as calculated using formula (7), identical to that for the image order ⑤'①②③④ (shown in Fig.5a), as the positions ⑤' and ⑤ share the same feature in the sinusoid curve, and the retrieved phase of the image order ⑤'①②③④ is the ordinate value of point T2 in Fig.5b. Similarly, the retrieved phases of image order ④⑤①②③, ③④⑤①②, and ②③④⑤① are equal to those of ④'⑤'①②③, ③'④'⑤'①② and ②'③'④'⑤'①, respectively, and the corresponding phase is the ordinate value of points T3, T4 and T5 in Fig.5d.

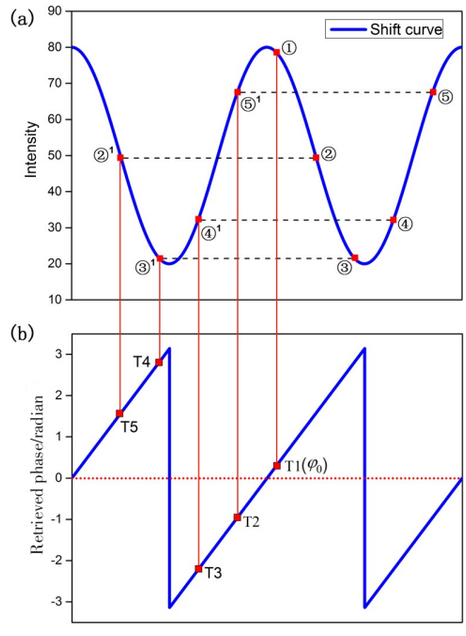

Fig.5 Schematic demonstration of the theory of cyclic shift operation on the raw images

For the case shown in Fig.5d, the retrieved phase of the 5 image orders can be calculated using formula (11):

$$\begin{aligned}
&\arg\{\text{background}①②③④⑤\} = \varphi_0;\\
&\arg\{\text{background}⑤①②③④\} =\\
&\quad \arg\{\text{background}⑤^{1}①②③④\} = \varphi_0 - \frac{2\pi}{5};\\
&\arg\{\text{background}④⑤①②③\} =\\
&\quad \arg\{\text{background}④^{1}⑤^{1}①②③\} = \varphi_0 - \frac{4\pi}{5};\\
&\arg\{\text{background}③④⑤①②\} =\\
&\quad \arg\{\text{background}③^{1}④^{1}⑤^{1}①②\} = \varphi_0 + \frac{4\pi}{5};\\
&\arg\{\text{background}②③④⑤①\} =\\
&\quad \arg\{\text{background}②^{1}③^{1}④^{1}⑤^{1}①\} = \varphi_0 + \frac{2\pi}{5}.
\end{aligned} \tag{11}$$

When the sample is placed in the beam path, based on the assumption that $\frac{2\pi}{d} z_T \varphi(x,y)$, which represents the phase shift introduced by the sample, is very tiny (e.g. - 0.001 radian), the phase of the pixel with sample in 5 orders of the images can be obtained using formula (12):

$$\begin{aligned}
&\arg\{\text{sample}①②③④⑤\} = \varphi_0 + \frac{2\pi}{d} z_T \varphi(x,y);\\
&\arg\{\text{sample}⑤①②③④\} =\\
&\quad \arg\{\text{sample}⑤^{1}①②③④\} = \varphi_0 + \frac{2\pi}{d} z_T \varphi(x,y) - \frac{2\pi}{5};\\
&\arg\{\text{sample}④⑤①②③\} =\\
&\quad \arg\{\text{sample}④^{1}⑤^{1}①②③\} = \varphi_0 + \frac{2\pi}{d} z_T \varphi(x,y) - \frac{4\pi}{5};\\
&\arg\{\text{sample}③④⑤①②\} =\\
&\quad \arg\{\text{sample}③^{1}④^{1}⑤^{1}①②\} = \varphi_0 + \frac{2\pi}{d} z_T \varphi(x,y) + \frac{4\pi}{5};\\
&\arg\{\text{sample}②③④⑤①\} =\\
&\quad \arg\{\text{sample}②^{1}③^{1}④^{1}⑤^{1}①\} = \varphi_0 + \frac{2\pi}{d} z_T \varphi(x,y) + \frac{2\pi}{5}.
\end{aligned} \tag{12}$$

Using background correction method based on arg(S)-arg(B) method, we have:

$$\begin{aligned}
&\arg\{\text{sample}①②③④⑤\} -\\
&\quad \arg\{\text{background}①②③④⑤\} = \frac{2\pi}{d} z_T \varphi(x,y);\\
&\arg\{\text{sample}⑤①②③④\} -\\
&\quad \arg\{\text{background}⑤①②③④\} = \frac{2\pi}{d} z_T \varphi(x,y);\\
&\arg\{\text{sample}④⑤①②③\} -\\
&\quad \arg\{\text{background}④⑤①②③\} = \frac{2\pi}{d} z_T \varphi(x,y);\\
&\arg\{\text{sample}③④⑤①②\} -\\
&\quad \arg\{\text{background}③④⑤①②\} = \frac{2\pi}{d} z_T \varphi(x,y);\\
&\arg\{\text{sample}②③④⑤①\} -\\
&\quad \arg\{\text{background}②③④⑤①\} = \frac{2\pi}{d} z_T \varphi(x,y).
\end{aligned} \tag{13}$$

Formula (13) shows that upon our assumption, when the order of the raw images with sample remains identical to that of the images without sample, the retrieved phase of the pure sample obtained with arg(S)-arg(B) method would be equal.

Fig.6 shows the computing process and the results using arg(S)- arg(B) method with different raw image orders. Fig.6A1, B1 and C1 show the computed phase with sample in the beam path, the phase without sample, and the pure phase of the sample after arg(S)- arg(B) operation with the image order of ①②③④⑤, respectively. In Fig.6, A2/B2/C2, A3/B3/C3, A4/B4/C4, and A5/B5/C5 show the computing process and results when the image sequence was ⑤①②③④, ④⑤①②③, ③④⑤①② and ②③④⑤①, respectively. Comparing the retrieved pure phase of the sample with the 5 different image orders, we found that in contrast with the theoretical analysis in formula (13), the retrieved image of the 5 orders were different due to the fact that in this experiment, the phase introduced by the sample was not that small as we assumed in formula (12).

Based on the observation in Fig.6C1-5, which show a constant variation of the areas where errors occur, we found that for a given pixel, error occurred in some sequences of the raw image but not in other sequences. For instance, the error occurred only at the bottom right in Fig.6C1 with the image order of ②③④⑤①. Further observation showed that the area of errors was constantly changing with the image sequence, suggesting that for a given pixel, at least one image sequence ensures that error does not occur.

Criteria can be established to identify the image sequence that ensures the lowest risk of error. In Fig.5b, the image order in which the initial phase without sample was located in the furthest area from the jump edge has the lowest risk of error, which means that the phase of the image sequence without sample positioned at the area closest to the red dash line possesses the lowest risk of error. This criteria is valid because it would be the safest condition to ensure that the subsequent phase with the contribution of the sample would not cross the jump edge even if can not predict the direction of the phase shift introduced by the sample, remembering that the jump edge is the ultimate source of error in arg(S)- arg(B) operation.

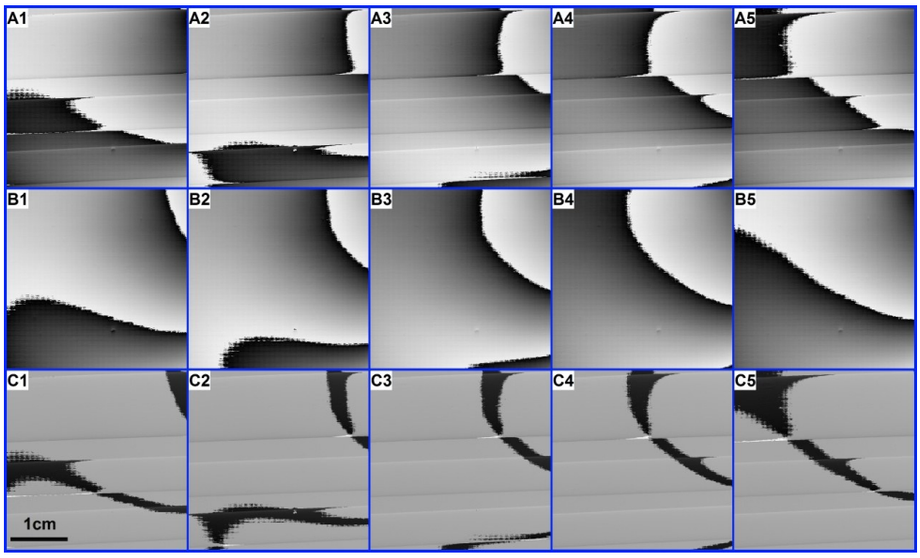

Fig.6 A1, B1and C1 show. the computing process and results of arg(S)-arg(B) method when the image sequence is ①②③④⑤. A1 is the phase with sample; B1 shows the phase without sample in the beam path; C1 depicts the phase after arg(S)-arg(B) operation. A2/B2/C2, A3/B3/C3, A4/B4/C4, and A5/B5/C5 show the computing process and outcomes for the image orders of ⑤①②③④, ④⑤①②③, ③④⑤①② and ②③④⑤①, respectively. All the images are windowed for optimized appearance with a linear gray scale.

Fig.6 Computing process and results using arg(S)−arg(B) method for the raw images with different orders

3.1 Novel algorithm for the method of [arg(S)-arg(B)] cyclic shift

Step 1: For the 5 orders of the raw images, calculating the phase images with and without sample, respectively:

$$\begin{aligned}
&\theta_1^b(x,y)=\arg\{\text{background①②③④⑤}\},\\
&\theta_1^s(x,y)=\arg\{\text{sample①②③④⑤}\};\\
&\theta_2^b(x,y)=\arg\{\text{background⑤①②③④}\},\\
&\theta_2^s(x,y)=\arg\{\text{sample⑤①②③④}\};\\
&\theta_3^b(x,y)=\arg\{\text{background④⑤①②③}\},\\
&\theta_3^s(x,y)=\arg\{\text{sample④⑤①②③}\};\\
&\theta_4^b(x,y)=\arg\{\text{background③④⑤①②}\},\\
&\theta_4^s(x,y)=\arg\{\text{sample③④⑤①②}\};\\
&\theta_5^b(x,y)=\arg\{\text{background②③④⑤①}\},\\
&\theta_5^s(x,y)=\arg\{\text{sample②③④⑤①}\}.
\end{aligned} \tag{14}$$

Step 2: For pixel (1, 1), indexing the minimum absolute value (k) in the 5 phase images without sample:

$$k=\text{Minimum index}\left[\left|\theta_1^b(1,1)\right|,\left|\theta_2^b(1,1)\right|,\left|\theta_3^b(1,1)\right|,\left|\theta_4^b(1,1)\right|,\left|\theta_5^b(1,1)\right|\right] \tag{15}$$

Step 3: Computing the refraction angle of pixel (1, 1):

$$\varphi(1,1)=\frac{d}{2\pi\times z_T}\times\left[\theta_k^s(1,1)-\theta_k^b(1,1)\right] \tag{16}$$

Step 4: For all the other pixels, repeating Step 2 and Step 3, and finally, obtaining the refraction image $\varphi(x,y)$.

3.2 Performance of the 4 methods

The data of 3 cylinders was the first case we took for evaluating the performance of the novel method, [arg(S)-arg(B)] cyclic shift. Fig7 shows the simulation results of the 3 cylinders by arg(S)-arg(B) method, arg(S/B) method, [arg(S)-arg(B)] modulo 2π and [arg(S)-arg(B)] cyclic shift, respectively.

Fig.8 shows the performance of the 4 methods in processing another more complex dataset. The sample was a chicken bone, and the raw images were collected with the same process as described previously. Fig.8 shows the simulation results of the chicken bone by arg(S)-arg(B) method, arg(S/B) method, [arg(S)-arg(B)] modulo 2π and [arg(S)-arg(B)] cyclic shift, respectively.

4 Discussion

Fig.7c and Fig.8c show that using the novel background correction methods, namely [arg(S)-arg(B)] modulo 2π and [arg(S)-arg(B)] cyclic shift, the phase wrapping due to arg(S)-arg(B) operation (as shown in Fig.7a and Fig.8a) was totally eliminated, and no visible difference was found between the images obtained by the new methods and arg(S/B) method. Numerical comparison (the histograms in Fig.7d and Fig.8d; the profiles in Fig.7e and Fig. 8e) also confirms that the novel

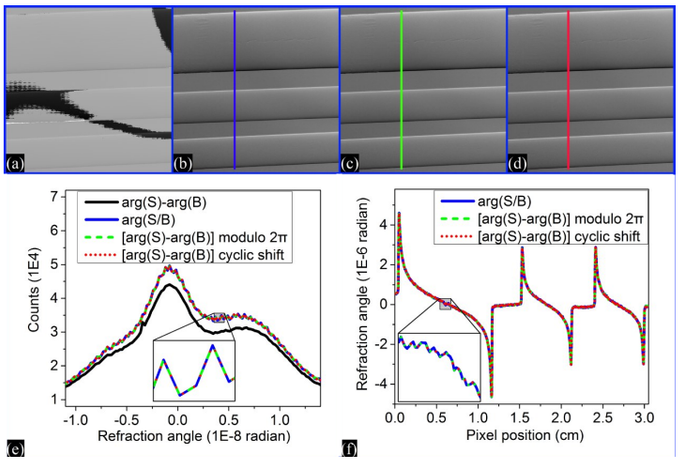

Fig.7a-d showed the retrieved image of three cylinders after the background correction with arg(S)-arg(B), arg(S/B), [arg(S)-arg(B)] modulo 2π, and [arg(S)-arg(B)] cyclic shift, respectively; Fig.7e was the histogram of Fig.7a-d, with the displayed refraction angle ranging from -1.1E-8 to 1.4E-8 radians, and the black curve, blue curve, green dotted curve and red dotted curve represented the histogram of the four different methods, respectively; Fig.7f was the refraction angle of the cross section chosen as shown in Fig.7b-d, respectively, and the blue curve, green dotted curve and red dotted curve stood for the data obtained with different methods. All the images were windowed for optimized appearance with a linear gray scale.

Fig.7 Refraction image of three cylinders after background correction

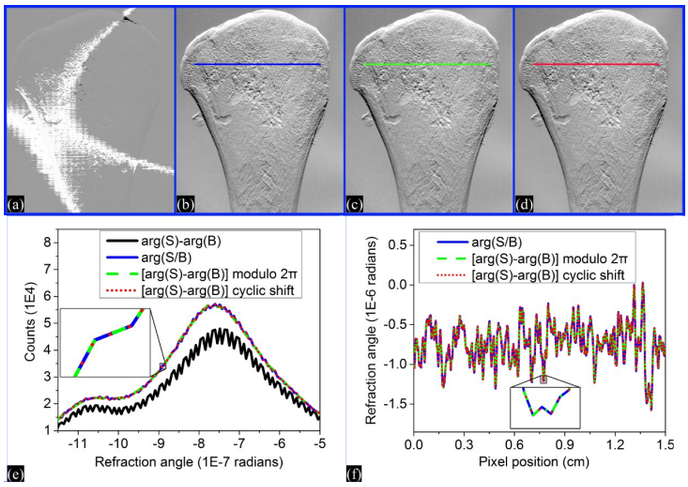

Fig.8a-d showed the refraction image of the chicken bone after the background correction with arg(S)-arg(B) method, arg(S/B) method, [arg(S)-arg(B)] modulo 2π, and the novel method, [arg(S)-arg(B)] cyclic shift. Fig.8e was the histogram of Fig.8a-d, with the selected refraction angle ranging from -11.5E-7 to -5E-7 radians, in which the black curve, blue curve, green dotted curve and the red dotted curve showed the histogram of the four methods respectively; Fig.8 was the refraction angle of the cross section chosen as shown in Fig.8b-d, and the blue curve, green dotted curve and red dotted curve represented the data obtained with different methods. All the images are windowed for optimized appearance with a linear gray scale.

Fig.8 Refraction image of the chicken bone after background correction

methods can successfully obtain exactly the same refraction signal as arg(S/B) method (see the enlarged view in Fig.7d, Fig.7e, Fig.8d and Fig.8e for details).

In our experiments, when using arg(S)- arg(B) method, the phase wrapping effect for some pixels that occurs only in some images results from the non-uniform initial phase of the background image (Fig.2). Phase wrapping occurs almost inevitably when the initial phase is located near the jump edge of the saw tooth curve (Fig.4b), indicating that the phase wrapping effect due to arg(S)-arg(B) operation is liable to occur where the gray value is located around the minimum in the first background image of the phase step-scan. The source of error in Fig.6C1 coincides with the darkest areas in Fig.2 (B ①), and that in Fig. 6(C2), Fig. 6(C3), Fig. 6(C4), Fig.6(C5) coincides with the darkest area in Fig.2(B ⑤),

Fig.2(B ④), Fig.2(B ③) and Fig. 2(B ②), respectively. During phase step-scan, when the analyzing grating moves, the darkest area (Moire fringe) shifts accordingly, and the area of error moves successively (Fig.6C1-5).

A possible advantage of [arg(S)-arg(B)] cyclic shift over arg(S/B) method is that the effective measuring range of the phase can be changed in some degree. For example, as shown in Fig.5b, when the initial phase of every pixel is tuned to point T1, the effective measuring range of [arg(S)-arg(B)] cyclic shift is $(-\varphi_0-\pi, -\varphi_0+\pi]$, and here we assume φ_0 is a positive and small value, such as $\frac{\pi}{10}$. If the initial phase of every pixel is tuned to point T3, the phase in the range of $\left(-\varphi_0-\frac{\pi}{5}, -\varphi_0+\frac{9\pi}{5}\right]$ can be measured by [arg(S)-arg(B)] cyclic shift without a phase wrapping effect, considering the fixed phase measuring range of (-π, π] in arg(S/B) method. If the desired phase of the sample is π+3, the measured phase of arg(S/B) method would be -π+3, and in this case, phase wrapping occurs and complicated phase unwrapping algorithm has to be used[23-27]. In contrast, a correct phase can be obtained with [arg(S)-arg(B)] cyclic shift when the measuring range is changed to $\left(-\frac{3\pi}{10}, \frac{17\pi}{10}\right]$.

For an easier implementation of the new background correction algorithm with computer, the first step in section 3.2 can be replaced by formula (17) without shifting the sequence of the raw images, while the other steps remain the same.

$$
\begin{aligned}
&\theta_1^b(x,y)=\arg\sum_{k=0}^{4}[I_{k+1}^b\times\exp(-i2\pi\frac{k}{5})],\\
&\theta_1^s(x,y)=\arg\sum_{k=0}^{4}[I_{k+1}^s\times\exp(-i2\pi\frac{k}{5})];\\
&\theta_2^b(x,y)=\arg\sum_{k=1}^{5}[I_{k}^b\times\exp(-i2\pi\frac{k}{5})],\\
&\theta_2^s(x,y)=\arg\sum_{k=1}^{5}[I_{k}^s\times\exp(-i2\pi\frac{k}{5})];\\
&\theta_3^b(x,y)=\arg\sum_{k=2}^{6}[I_{k-1}^b\times\exp(-i2\pi\frac{k}{5})],\\
&\theta_3^s(x,y)=\arg\sum_{k=2}^{6}[I_{k-1}^s\times\exp(-i2\pi\frac{k}{5})];\\
&\theta_4^b(x,y)=\arg\sum_{k=3}^{7}[I_{k-2}^b\times\exp(-i2\pi\frac{k}{5})],\\
&\theta_4^s(x,y)=\arg\sum_{k=3}^{7}[I_{k-2}^s\times\exp(-i2\pi\frac{k}{5})];\\
&\theta_5^b(x,y)=\arg\sum_{k=4}^{8}[I_{k-3}^b\times\exp(-i2\pi\frac{k}{5})],\\
&\theta_5^s(x,y)=\arg\sum_{k=4}^{8}[I_{k-3}^s\times\exp(-i2\pi\frac{k}{5})].
\end{aligned}
\tag{17}
$$

This step is identical to step 1 in section 3.1 because:

$$
\begin{aligned}
\theta_2(x,y)&=\left[\underbrace{\arg\sum_{k=0}^{4}[I_{k+1}\times\exp(-i2\pi\frac{k}{5})]}_{\text{sequence}=⑤①②③④}\right]\\
&=\left[\underbrace{\arg\sum_{k=1}^{5}[I_{k}\times\exp(-i2\pi\frac{k}{5})]}_{\text{sequence}=①②③④⑤}\right];\\
\theta_3(x,y)&=\left[\underbrace{\arg\sum_{k=0}^{4}[I_{k+1}\times\exp(-i2\pi\frac{k}{5})]}_{\text{sequence}=④⑤①②③}\right]\\
&=\left[\underbrace{\arg\sum_{k=2}^{6}[I_{k-1}\times\exp(-i2\pi\frac{k}{5})]}_{\text{sequence}=①②③④⑤}\right];\\
\theta_4(x,y)&=\left[\underbrace{\arg\sum_{k=0}^{4}[I_{k+1}\times\exp(-i2\pi\frac{k}{5})]}_{\text{sequence}=③④⑤①②}\right]\\
&=\left[\underbrace{\arg\sum_{k=3}^{7}[I_{k-2}\times\exp(-i2\pi\frac{k}{5})]}_{\text{sequence}=①②③④⑤}\right];\\
\theta_5(x,y)&=\left[\underbrace{\arg\sum_{k=0}^{4}[I_{k+1}\times\exp(-i2\pi\frac{k}{5})]}_{\text{sequence}=②③④⑤①}\right]\\
&=\left[\underbrace{\arg\sum_{k=4}^{8}[I_{k-3}\times\exp(-i2\pi\frac{k}{5})]}_{\text{sequence}=①②③④⑤}\right].
\end{aligned}
\tag{18}
$$

In order to reduce memory consumption of the computer by the algorithm, another algorithm is available and shown as the following:

Step 1: For pixel (1, 1), indexing the maximum value of gray value in the 5 raw images without sample as this:

$$
n=\text{Maximum index}\begin{bmatrix}I_1^b(1,1), I_2^b(1,1), I_3^b(1,1),\\ I_4^b(1,1), I_5^b(1,1)\end{bmatrix}, 1\leqslant n\leqslant 5 \tag{19}
$$

Step 2: Computing the refraction angle of pixel (1, 1) as:

$$
\varphi(1,1)=\frac{d}{2\pi\times z_T}\times\begin{bmatrix}\arg\sum_{k=1-n}^{5-n}[I_k^s\times\exp(-i2\pi\frac{k}{5})]-\\ \arg\sum_{k=1-n}^{5-n}[I_k^b\times\exp(-i2\pi\frac{k}{5})]\end{bmatrix} \tag{20}
$$

Step 3: For all the other pixels, repeating Step 1 and Step 2, and finally obtaining the refraction image $\varphi(x,y)$.

The rationale of this algorithm is identical to that of the aforementioned algorithm. As shown in Fig.5a, when

the gray value in the first step is the maximum, the initial phase of the pixel without sample would occur in the farthest area from the jumping edge. The advantage of this algorithm is that phase is computed only once (which lowers memory consumption of the computer), as compared with 5 times with the aforementioned algorithms.

This novel background correction method can also be used in other techniques, such X-ray phase contrast imaging with a crystal X-ray interferometer[4-6], and phase measurement technique with visible light [29].

Acknowledgements: The authors are grateful to Margie P. Olbinado, Atsushi Momose, Murakami Gaku, Wataru Abe, Taiki Umemoto and Kosuke Kato (Institute of Multidisciplinary Research for Advanced Materials, Tohoku University, 2- 1- 1Katahira, Aoba- ku, Sendai, Miyagi 980-8577, Japan) for their generous help with the experiments. This study was financially supported by Japan- Asia Youth Exchange program in Science (SAKURA Exchange Program in Science) administered by the *Japan Science and Technology Agency.*

References

[1] LEWIS R A. Medical phase contrast X-ray imaging: current status and future prospects[J]. Phys Med Biol, 2004, 49(16): 3573-3583.

[2] MOMOSE A. Recent advances in X-ray phase imaging[J]. Jpn J Appl Phys, 2005, 44(9A): 6355.

[3] ZHOU S A, BRAHME A. Development of phase- contrast X- ray imaging techniques and potential medical applications[J]. Phys Med, 2008, 24(3): 129-148.

[4] BONSE U, HART M. An X-ray interferometer[J]. Appl Phys Lett, 1965, 6(8): 155-156.

[5] MOMOSE A. Demonstration of phase- contrast X- ray computed tomography using an X-ray interferometer[J]. Nucl Instrum Meth A, 1995, 352(3): 622-628.

[6] MOMOSE A, TAKEDA T, ITAI Y, et al. Phase-contrast X-ray computed tomography for observing biological soft tissues[J]. Nat Med, 1996, 2(4): 473-475.

[7] WILKINS S, GUREYEV T, GAO D, et al. Phase-contrast imaging using polychromatic hard X-rays[J]. Nature, 1996, 384(6607): 335-338.

[8] NUGENT K, GUREYEV T, COOKSON D, et al. Quantitative phase imaging using hard X rays[J]. Phys Rev Lett, 1996, 77(14): 2961.

[9] DAVIS T, GAO D, GUREYEV T, et al. Phase-contrast imaging of weakly absorbing materials using hard X-rays[J]. Nature, 1995, 373 (373): 595-598.

[10] CHAPMAN D, THOMLINSON W, JOHNSTON R, et al. Diffraction enhanced X-ray imaging[J]. Phys Med Biol, 1997, 42(11): 2015-2025.

[11] DAVID C, NÖHAMMER B, SOLAK H H, et al. Differential X-ray phase contrast imaging using a shearing interferometer[J]. Appl Phys Lett, 2002, 81(17): 3287-3289.

[12] MOMOSE A, KAWAMOTO S, KOYAMA I, et al. Demonstration of X-ray Talbot interferometry[J]. Jpn J Appl Phys, 2014, 42(Part2): L866-L868.

[13] MOMOSE A, YASHIRO W, TAKEDA Y, et al. Phase tomography by X-ray Talbot interferometry for biological imaging[J]. Jpn J Appl Phys, 2014, 45(6A): 5254.

[14] PFEIFFER F, WEITKAMP T, BUNK O, et al. Phase retrieval and differential phase-contrast imaging with low-brilliance X-ray sources [J]. Nat Phys, 2006, 2: 258-261.

[15] PFEIFFER F, KOTTLER C, BUNK O, et al. Hard X- ray phase tomography with low-brilliance sources[J]. Phys Rev Lett, 2007, 98 (10): 108105.

[16] PFEIFFER F, BECH M, BUNK O, et al. Hard- X- ray dark- field imaging using a grating interferometer[J]. Nat Mater, 2008, 7(2): 134-137.

[17] STUTMAN D, BECK T J, CARRINO J A, et al. Talbot phase-contrast X-ray imaging for the small joints of the hand[J]. Phys Med Biol, 2011, 56(17): 5697-5720.

[18] ZANETTE I, WEITKAMP T, LEDUC G, et al. X-ray grating-based phase tomography for 3D histology[J]. RSC Adv, 2013, 3(43): 19816-19819.

[19] BECH M, TAPFER A, VELROYEN A, et al. *In-vivo* dark-field and phase-contrast X-ray imaging[J]. Sci Rep-UK, 2013, 3(3): 3209.

[20] TANAKA J, NAGASHIMA M, KIDO K, et al. Cadaveric and *in vivo* human joint imaging based on differential phase contrast by X-ray Talbot-Lau interferometry[J]. Z Med Phys, 2013, 23(3): 222-227.

[21] MOMOSE A, YASHIRO W, KIDO K, et al. X-ray phase imaging: from synchrotron to hospital[J]. Philos T Royal Soc A, 2014, 372(2010): 20130023.

[22] ZANETTE I. Interférométrie X à réseaux pour l'imagerie et l'analyse de front d'ondes au synchrotron[D]. Grenoble: Université Grenoble Alpes, 2011.
ZANETTE I. X-ray interferometry for wavefront imaging and analysis at the synchrotron[D]. Grenoble: University of Grenoble Alpes, 2011.

[23] ITOH K. Analysis of the phase unwrapping algorithm[C]. Appl Optics, 1982, 21(14): 2470.

[24] JUDGE T R, BRYANSTON-CROSS P. A review of phase unwrapping techniques in fringe analysis[J]. Opt Laser Eng, 1994, 21(4): 199-239.

[25] HAAS W, BECH M, BARTL P, et al. Phase-unwrapping of differential phase- contrast data using attenuation information[J]. SPIE Med Imaging, 2011, 7962(3): 298-306.

[26] JERJEN I, REVOL V, SCHUETZ P, et al. Reduction of phase artifacts in differential phase contrast computed tomography[J]. Opt Express, 2011, 19(14): 13604-13611.

[27] EPPLE F M, POTDEVIN G, THIBAULT P, et al. Unwrapping differential X-ray phase- contrast images through phase estimation from multiple energy data[J]. Opt Express, 2013, 21(24): 29101-29108.

[28] BRUNING J, HERRIOTT D R, GALLAGHER J, et al. Digital wavefront measuring interferometer for testing optical surfaces and lenses[J]. Appl Optics, 1974, 13(11): 2693.

[29] CREATH K. Phase-measurement interferometry techniques[J]. Prog Optics, 1988, 26: 349-393.

[30] WEITKAMP T, DIAZ A, DAVID C, et al. X-ray phase imaging with a grating interferometer[J]. Opt Express, 2005, 13(16): 6296-6304.

（编辑：谭斯允）

医学影像物理

X射线光栅相位衬度成像技术中背景扣除方法的比较

杨萌[1],胡仁芳[1],王圣浩[2],吴朝[1],田扬超[1]
1.中国科学技术大学国家同步辐射实验室,安徽 合肥230027;2.中国科学院上海光学精密机械研究所检测中心,上海 201800

【摘 要】在基于Talbot-Lau干涉仪的X射线相位衬度成像技术中,为了得到纯样品的相位信息,背景扣除是一个必不可少的步骤。本研究对相位衬度成像中的背景扣除方法进行了研究,尤其是针对目前经常使用的一种背景扣除方法,提出了一种新的相位解缠绕方案,即[arg(S)-arg(B)] cyclic shift算法,该方案的核心思想是对原始图像序列进行循环移位操作,从而达到改变相位的目的。实验结果和数值分析表明,该相位解缠绕方案可以完全消除上述背景扣除方法中的相位缠绕现象。同时,基于这种方案,相位的有效测量范围可以根据情况灵活调节,如调为(-π+3, π+3],而目前常用背景扣除方法的相位测量范围都是固定在(-π, π]。

【关键词】X射线成像;Talbot-Lau干涉仪;背景扣除;循环移位;相位解缠绕
【中图分类号】O434.11 【文献标志码】A 【文章编号】1005-202X(2017)07-0649-11

【收稿日期】2017-03-14
【基金项目】国家重大科研装备研制项目(CZBZDYZ20140002);中央高校基本科研业务费专项资金(WK2310000065)
【作者简介】杨萌,男,硕士研究生,研究方向:X射线相位衬度成像,E-mail: henry@mail.ustc.edu.cn;胡仁芳,男,博士研究生,研究方向:X射线相位衬度成像,E-mail:hurf@mail.ustc.edu.cn
【通信作者】田扬超,E-mail:ychtian@ustc.edu.cn;王圣浩,男,博士,助理研究员,研究方向:X射线相位衬度成像,E-mail: wangshenghao@siom.ac.cn